Journal of MATERIALS RESEARCH

Article
DOI: 10.1557/jmr.2019.217

Precipitation behavior of dispersoids and elevated-temperature properties in Al–Si–Mg foundry alloy with Mo addition

S. Chen[1], K. Liu[1,a)], X-G. Chen[1]

[1]*Department of Applied Sciences, University of Québec at Chicoutimi, Chicoutimi, QC G7H 2B1, Canada*

[a)]Address all correspondence to this author. kun.liu@uqac.ca

Received: 15 January 2019; accepted: 4 June 2019

In the present work, Mo was added to an Al–Si–Mg foundry alloy to study its influence on the evolution of dispersoids during various heat treatments. The microhardness and the elevated-temperature tensile properties and creep resistance were measured to evaluate the contribution of dispersoids. Results showed that the addition of Mo greatly promoted the formation of α-dispersoids. During solution treatment, the formation of α-dispersoids started after 8 h at 500 °C. At high temperature (540 °C), the coarsening of dispersoids with increasing time became predominant. The optimum condition of dispersoids can be reached by 520 °C/12 h or 500 °C/4 h + 540 °C/2 h, leading to the highest differences in microhardness between the Mo-containing alloy and base alloy. The tensile strengths were improved at both room temperature and elevated temperatures, while the elongation at elevated temperature was greatly increased. The creep resistance at elevated temperature is further enhanced due to the Mo addition.

Introduction

A significant increase in the usage of aluminum foundry alloys to replace cast iron in aerospace and automotive industries has been witnessed in decades due to their high strength-to-weight ratio, good corrosion resistance, and excellent castability [1, 2, 3]. One of the examples is the application of Al–Si–Mg foundry alloys in cylinder heads and engine blocks due to the increasing demand for lightweight vehicles [4, 5].

Generally, Al–Si–Mg foundry alloys are classified to age-hardening aluminum alloys due to the fine nano-scale precipitates formed during the artificial aging process after solution treatment. Recent research works have focused on optimizing the properties of Al–Si foundry alloys by Mg and Cu additions to form β′-Mg_2Si and θ′-Al_2Cu precipitates [6, 7, 8, 9]. It is reported that proper addition of Cu (1–1.5 wt%) can enhance the mechanical properties of Al–Si–Mg alloy by increasing the density of β″ precipitates [9]. Unfortunately, a severe drop in strength is found when the components are exposed to elevated temperatures, such as 250–350 °C, due to the rapid coarsening of these precipitates [10]. Therefore, attentions have been drawn to the improvement of elevated-temperature properties in Al–Si–Mg foundry alloys, especially on the automobile applications, such as cylinder head and engine block components.

One of the practical solutions to improve elevated-temperature properties of aluminum alloys is to introduce a large amount of thermally stable dispersoids via adding rare earth elements or transition elements [11, 12]. In our previous study on the elevated-temperature behavior of Al–Mn–Mg 3004 alloys [13, 14], it is found that the thermally stable α-Al(Fe,Mn)Si dispersoids can be formed with fine size and high volume fraction by adjusting alloying elements, such as Fe, Mn, and Cu, leading to a remarkable improvement in the strength and creep resistance at 300 °C. Investigations have been performed to study the formation, growth, and coarsening behavior of dispersoids at elevated temperature [15, 16, 17]. Li et al. [18] reported two possible orientation relationships between Al matrix and α-Al(Fe,Mn)Si dispersoids and studied the thermal stability of the dispersoids. Lodgaard et al. [19] studied the effect of the heating procedure on dispersoid distribution and concluded that the slow heating rate could result in uniform and high density of dispersoids. Crystal structure and morphology of dispersoids are determined by Kim et al. [20]. Li and Arnberg [21] also quantitatively studied

https://doi.org/10.1557/jmr.2019.217 Published online by Cambridge University Press

© Materials Research Society 2019

the precipitation behavior of Mn-containing dispersoids during heating and homogenization processes. Moreover, the effects of dispersoids on tensile properties [22, 23] and fatigue properties [24, 25] of Al–Zn–Mg alloy have been studied. Improvements were witnessed for mechanical properties due to the presence of α-Al(Fe,Mn)Si dispersoids.

However, limited literature can be found on the effect of dispersoids in Al–Si–Mg foundry alloys. Farkoosh et al. [26, 27] reported that Mo, combining with Mn, had great potential to form a large amount of dispersoids in Al–Si–Mg alloys and could improve elevated-temperature properties. However, the precipitation behavior of dispersoids during heat treatment was unclear. In the present work, the precipitation behavior of dispersoids in Al–Si–Mg 356-type alloys during heat treatments with various temperatures and soaking times was systematically studied. The evolution of dispersoids during heat treatment was characterized by their size and number density and was further confirmed by the microhardness changes. Furthermore, the role of Mo-containing dispersoids in tensile properties at room and elevated temperatures and the creep resistance at 300 °C was also evaluated.

Results and discussion

Microstructure in as-cast and solution-treated conditions

Figure 1 shows the as-cast microstructures of experimental 356NM and 356M alloys. As can be seen, the microstructures of both alloys are similar, which were consisted of α-Al dendrites, refined eutectic Si particles, and various intermetallic phases located in the interdendrite regions. The secondary dendrite arm spacing was measured to be 30 ± 8 μm for 356NM alloy and 31 ± 8 μm for 356M alloy. Figures 1(b) and 1(d) show the detailed information of various intermetallics. Two kinds of Fe-containing phases [α-Al(Fe,Mn)Si and π-$Al_8FeMg_3Si_6$], two Cu-containing phases (Q-$Al_5Cu_2Mg_8Si_6$ and θ-Al_2Cu), and Mg_2Si are all found in both alloys, while a small amount of Mo is detected in α-Al(Fe,Mn)Si intermetallics in 356M alloy [Fig. 1(d)]. One thing to be mentioned that no platelet/needle-like β-Al_5FeSi phase was observed in both 356NM and 356M alloys. This can be attributed to a relatively high amount of Mn in 356NM and 356M alloys, which was reported to effectively promote the transformation from β-Al_5FeSi to α-Al(Fe,Mn)Si [28, 29]. In addition, Mo was also reported to modify the β-Fe to α-Fe in Al–Si 356 alloys [26, 30]. Hence, it is reasonable to expect the α-Al(Fe,Mn)Si rather than β-Al_5FeSi in two experimental alloys.

During solution treatment, the eutectic Si particles were spheroidized, while primary Mg_2Si, Q-$Al_5Cu_2Mg_8Si_6$, and θ-Al_2Cu intermetallics presented in the as-cast microstructure were gradually dissolved in the aluminum matrix with increasing temperature and soaking time for both alloys. The microstructure of both alloys after solution treatment at 540 °C for 8 h is shown in Fig. 2 as one example. As can be seen that the eutectic Si particles are much smaller and spheroidized than that in as-cast condition. On the other hand, fine dispersoids

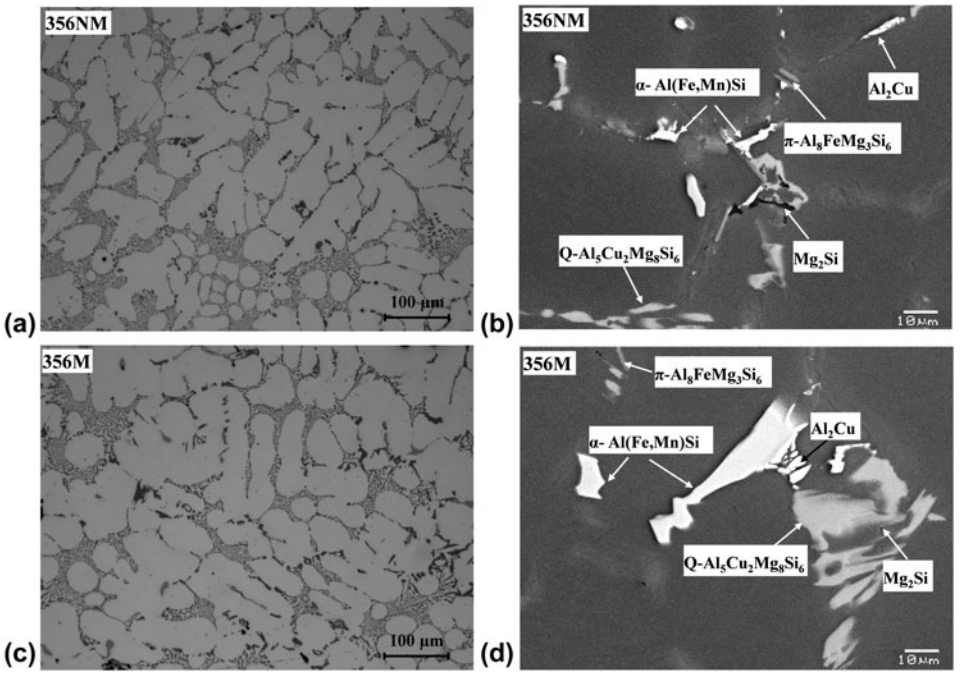


Figure 1: As-cast microstructure of experimental alloys: (a, b) 356NM and (c, d) 56M.

https://doi.org/10.1557/jmr.2019.217 Published online by Cambridge University Press

© Materials Research Society 2019

were formed and distributed in the intradendritic region of 356NM and 356M alloys. It can be seen that only a few of dispersoids appeared in the matrix of 356NM alloy [Fig. 2(a)], while a large number of dispersoids formed in the matrix in 356M alloy [Fig. 2(b)], which were centered inside aluminum cells. The number density of dispersoids is much higher in 356M than in 356NM alloy, indicating that the addition of Mo greatly promotes the formation of dispersoids. Meanwhile, the dispersoid-free zone (DFZ) can be observed between two adjacent dispersoid zones. The segregation of Mo in the centers of aluminum dendrites due to its partition coefficient larger than unity (k_{Mo} = 2.5 [31]) results in the origin of DFZ. Meanwhile, the coarsening between the fine dispersoids and coarse constituent particles/intermetallics during the solution treatment can also result in the formation of DFZ [21, 32].

Transmission electron microscope (TEM) observation was performed on those fine dispersoids in Fig. 2. They were all identified as α-Al(Fe,Mn/Mo)Si dispersoids and hence "α-dispersoids" is used in the following text. The TEM analysis in 356M alloy is shown in Fig. 3 as an example. The diameter of

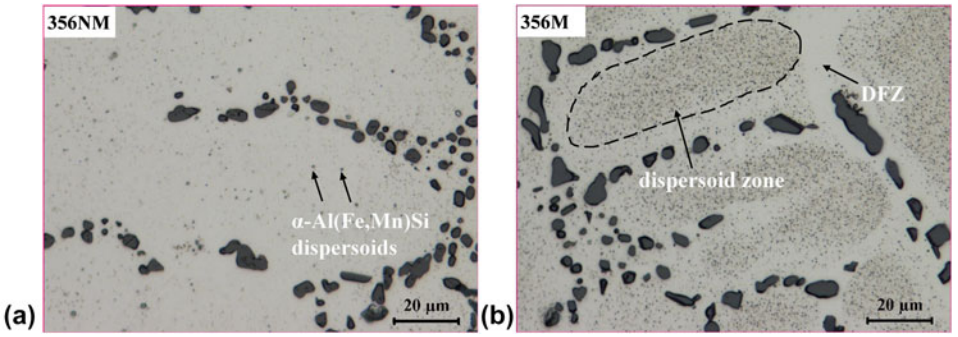


Figure 2: OM images of experimental alloys after 8 h solution treatment at 540 °C: (a) 356NM and (b) 356M alloys.

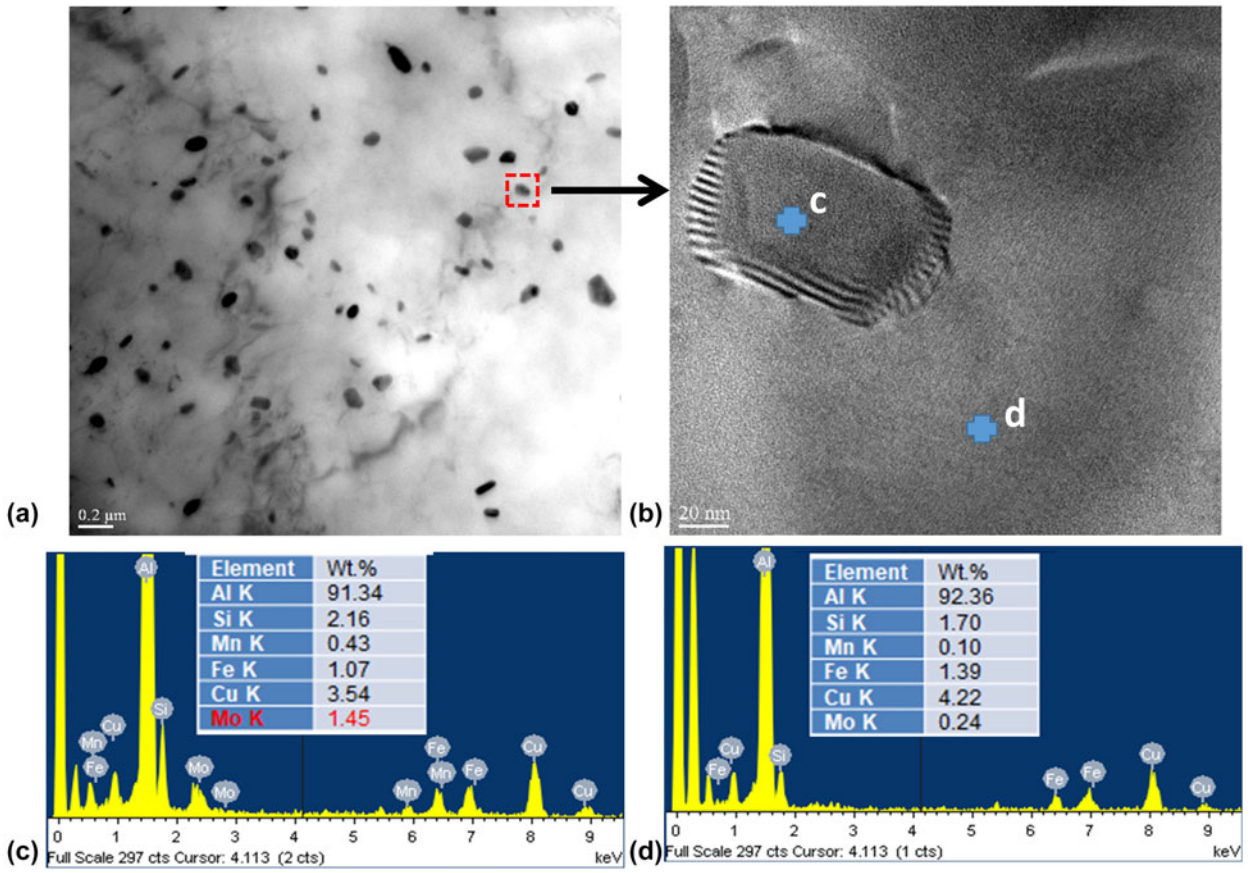


Figure 3: The (a) distribution and (b) morphology of α-dispersoids and TEM-EDS result of (c) α-dispersoids and (d) matrix in 356M alloy.

https://doi.org/10.1557/jmr.2019.217 Published online by Cambridge University Press

© Materials Research Society 2019

α-dispersoids is approximately 100 nm [Fig. 3(a)] and the semi-coherent boundary between α-dispersoids and Al matrix can be observed in Fig. 3(b). Figures 3(c) and 3(d) show the TEM-EDS (energy-dispersive X-ray spectroscopy) results of α-dispersoids and surrounding matrix in 356M alloy. It can be found the content of Si, Mn, and Mo is much higher in α-dispersoids than in the matrix: 2.16%, 0.43%, and 1.45% in α-dispersoids compared with 1.7%, 0.1%, and 0.24% in matrix, respectively, further confirming the composition of α-dispersoids with Mn and Mo.

Evolution of α-dispersoids during solution treatment

As shown in Fig. 2, a large number of α-dispersoids in 356M alloy but a few of big ones in 356 NM can be observed after 540 °C/8 h, indicating the different formation behaviors of dispersoids in two alloys. Therefore, the solution treatment under various conditions (see Experimental procedures section) was applied to study the effect of temperature and soaking time on the evolution of dispersoids. The general tendency of the dispersoid evolution with increasing solution temperature for 24 h is presented in Fig. 4. It can be observed that the number density of α-dispersoids increased when the temperature increases from 500 °C [Fig. 4(a)] to 520 °C [Fig. 4(b)], and however, the number density of α-dispersoids moderately decreased when the temperature further increases to 540 °C [Fig. 4(c)].

The Vickers microhardness measurements were carried out on both experimental alloys right after the solution heat treatment. To clearly show the general tendency and the differences between two alloys, the evolution of hardness with temperature in 356NM and the differences of Vickers microhardness (ΔHV) of 356NM and 356M during the solution treatment at various temperatures are shown in Fig. 5. As shown in Fig. 5(a), the microhardness of 356NM keeps almost unchanged at 500 °C and starts to increase at higher temperatures (520 and 540 °C) with increasing holding time, principally due to the dissolution of primary Mg_2Si and Al_2Cu. On the other hand, it can be found the ΔHV is always positive in Fig. 5(b), indicating the higher hardness in 356M than that in 356NM. Because ΔHV is greatly related to the condition of the aluminum matrix, especially to the decomposition of supersaturated solid solution to form dispersoids, the tendency of ΔHV can be considered as a clear indicator for the evolution of α-dispersoids in 356M alloy. As shown in Fig. 5(b), different tendencies can be observed under various temperatures. When treated at 500 °C, ΔHV is very low in the first 4 h and then

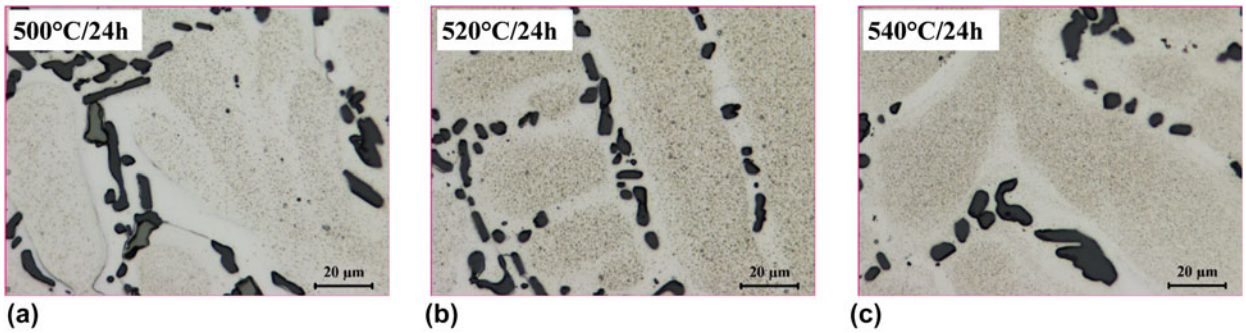


Figure 4: The precipitation of dispersoids in 356M alloy during solution treatment for 24 h at (a) 500 °C, (b) 520 °C, and (c) 540 °C.

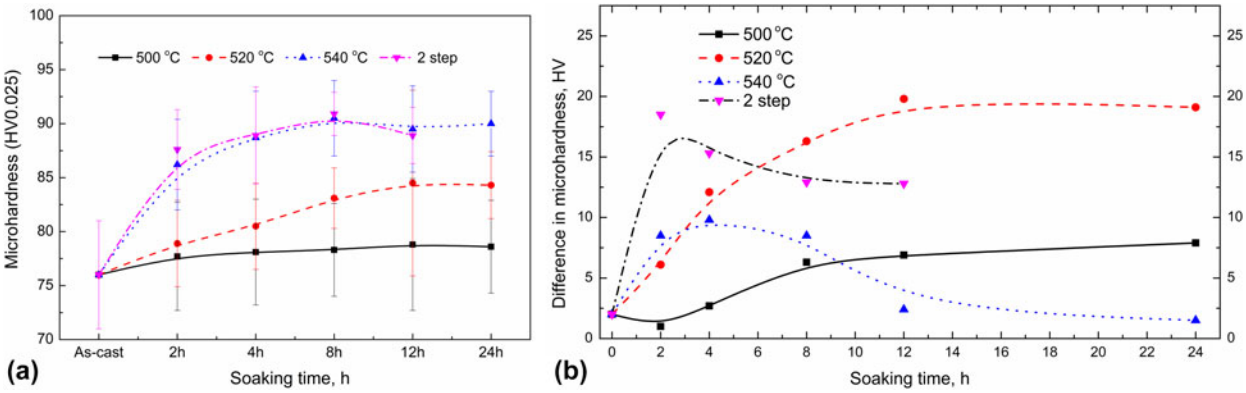


Figure 5: (a) Evolution of microhardness in 356NM and (b) differences in microhardness (ΔHV) between 356NM and 356M during solution treatment at various temperatures.

https://doi.org/10.1557/jmr.2019.217 Published online by Cambridge University Press

Journal of Materials Research ■ Volume 34 ■ Issue 18 ■ Sep 30, 2019 ■ www.mrs.org/jmr

© Materials Research Society 2019

slowly increases with increasing soaking time. After 8 h, it reaches a plateau. At 520 °C, ΔHV rapidly increases to the peak value after 12 h, followed by a plateau. At this temperature, the highest ΔHV of ~20 HV is obtained, which is 25% improvement compared with that in 356NM [83 HV max. at 520 °C in Fig. 5(a)]. With further increasing solution temperature to 540 °C, ΔHV rapidly increases to the peak value after 4 h, after that it starts to decrease with increasing holding time. As for the two-step solution treatment, the highest ΔHV appears at 2 h at 540 °C and the peak value reaches the same level as that of 520 °C/12 h. Followed by the peak, there is a gradual drop in ΔHV. Since the formation of dispersoids is very weak in the base alloy (356NM) in all solution treatment conditions applied, as shown in Fig. 2(a), only the evolution of dispersoids in 356M alloy is discussed in detail in the following section.

Figure 6 shows the evolution of the number density and average equivalent diameter of α-dispersoids during solution treatment at different temperatures, analyzed by image analysis on a series of scanning electron microscopy (SEM) images as shown in Fig. 7. As shown in Fig. 6(a), when treated at 500 °C, the formation of dispersoids is hardly observed until 8 h. After 8 h, the dispersoids are visible under SEM, and the number density of dispersoids increases slowly with increasing soaking time. The average size of dispersoids is approximately 100 nm. It is apparent that the formation of dispersoids after 8 h results in an increase in ΔHV in Fig. 5. After 24 h, the number density and average size of dispersoids still keep at a low level. Therefore, the increase in ΔHV is limited (5–8 HV) at 500 °C. It can be concluded that the kinetics of the dispersoid formation is quite slow at such temperature and it needs a long incubation time to form Mo-containing α-dispersoids, most likely attributing to a low diffusion coefficient of Mo in aluminum at 500 °C (1.8×10^{-20} m^2/s [33]).

With increasing solution temperature to 520 °C [Fig. 6(b)], a number of dispersoids can be clearly observed during first 2–4 h soaking. After 4 h, the number density of dispersoids increases rapidly with increasing soaking time, indicating a full precipitation of dispersoids. During solution treatment, the average dispersoid size increases gradually from 120 nm (after 2 h) to 150 nm (after 24 h). It is evident that the kinetics of the dispersoid formation here is more favorable than at 500 °C, because the diffusion coefficient of Mo in aluminum at 520 °C

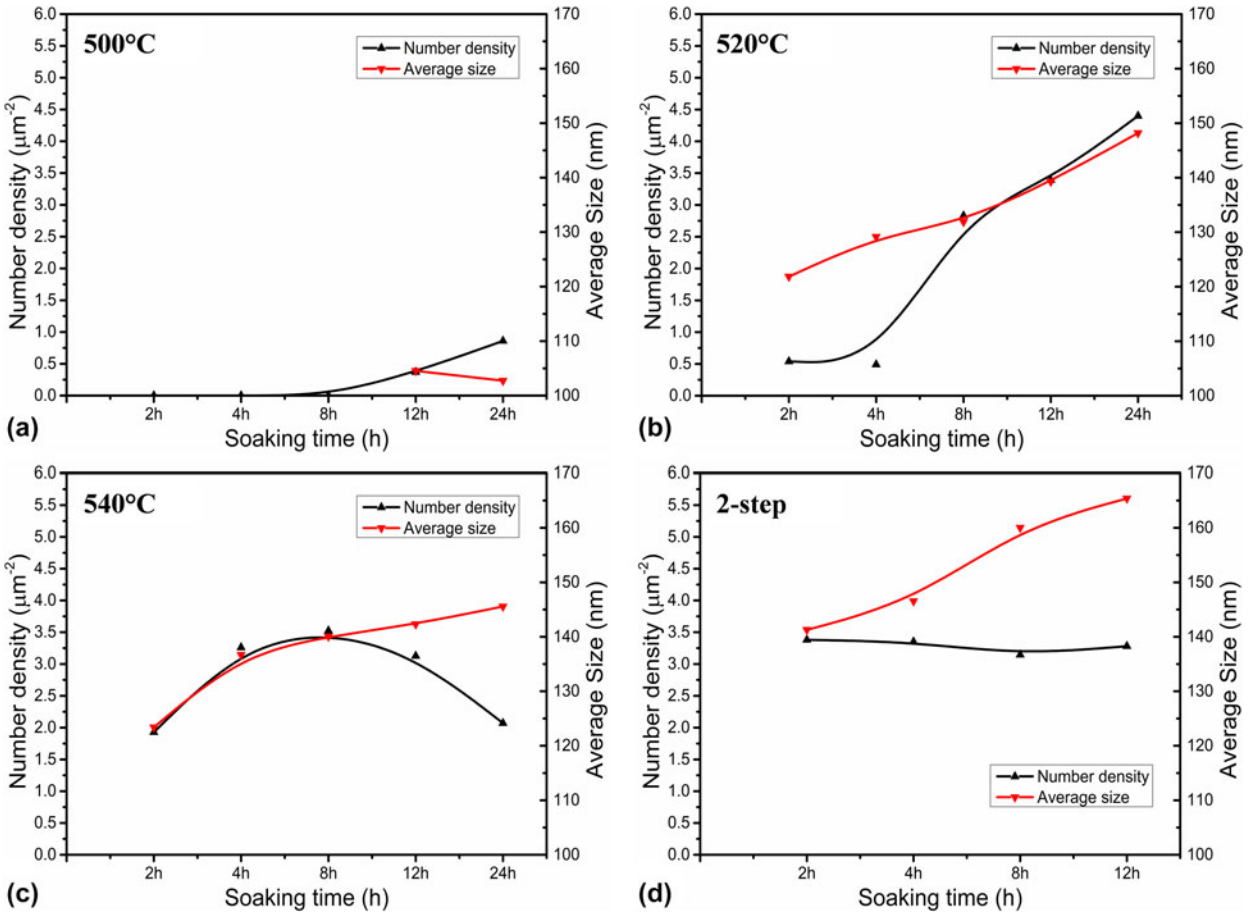


Figure 6: Evolution of number density and average size of dispersoids during solution heat treatment at (a) 500 °C, (b) 520 °C, (c) 540 °C, and (d) 2-step.

https://doi.org/10.1557/jmr.2019.217 Published online by Cambridge University Press

© Materials Research Society 2019

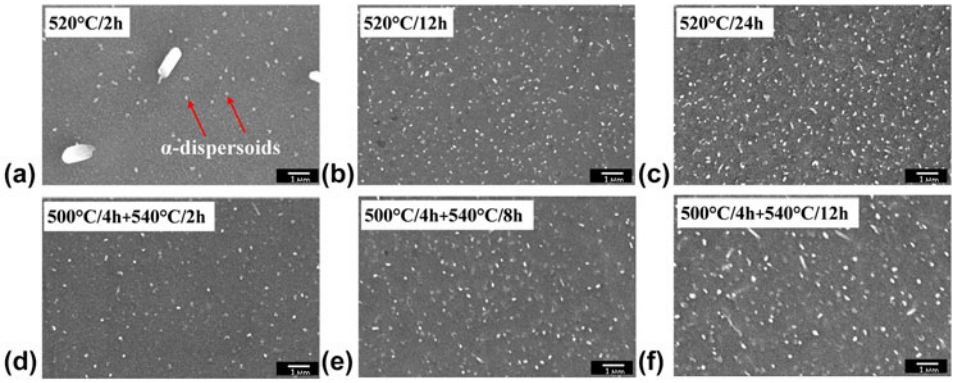


Figure 7: Dispersoid evolution during solution treatment at (a) 520 °C/2 h, (b) 520 °C/12 h, (c) 520 °C/24 h, (d) 500 °C/4 h + 540 °C/2 h, (e) 500 °C/4 h + 540 °C/8 h, and (f) 500 °C/4 h + 540 °C/12 h.

(1.9×10^{-19} m^2/s [33]) is ten times higher than that at 500 °C (1.8×10^{-20} m^2/s). The evolution of dispersoids in Fig. 6(b) also well explains the tendency of ΔHV at 520 °C shown in Fig. 5. The formation of dispersoids with increasing number density leads to the increasing ΔHV until it reaches the peak value at 12 h. As shown in Fig. 6(b), the number density of dispersoids is much higher after 520 °C/12 h than that after 500 °C/24 h. Therefore, the peak value of ΔHV is much higher at 520 °C/12 h than at 500 °C/24 h (20 HV versus 7 HV), confirming a remarkable contribution of α-dispersoids to the strength. After that, the plateau on the ΔHV is attributed to the balance between the increasing number density and coarsening of dispersoids.

The evolution of α-dispersoids at 540 °C is shown in Fig. 6(c). The number density of dispersoids increases gradually during the first 8 h soaking, which contributes to the rapid increasing of ΔHV in Fig. 5. After 8 h, the coarsening of dispersoids becomes the main mechanism, which leads to a quick drop in the number density and a sustainable increase in particle size. The decline of ΔHV after 8 h also reflects the time point when coarsening becomes obvious. With increasing temperature to 540 °C, the diffusion coefficient of Mo is significantly enhanced to be 4.6×10^{-19} m^2/s, which makes Ostwald ripening possible between dispersoids, resulting in a decrease in the number density and an increase in the dispersoid size.

Figure 6(d) illustrates the evolution of dispersoids during two-step solution treatment. During the first 2 h soaking, the highest number density of dispersoids is already observed relative to other three solution treatments at the same soaking time. It indicates that the first step of treatment (500 °C/4 h) provides a good incubation time for the nucleation of dispersoids. During the second step of treatment at 540 °C, the dispersoids can quickly grow out in the matrix in a short period. With increasing soaking time at the second step, the number density of dispersoids remains more and less constant, while the average dispersoid size increases gradually. The maximum ΔHV value appears after 2 h when the dispersoid diameter is the smallest during soaking (Fig. 6). After that, the continuous increase in the dispersoid size causes a gradual decrease of ΔHV.

As can be seen in Fig. 5, the maximum ΔHV value is obtained at 520 °C/12 h and 500 °C/4 h + 540 °C/2 h. Therefore, the dispersoid evolutions during 520 °C (one step) and 500 °C/4 h + 540 °C (2 steps) treatments are illustrated in detail (Fig. 7). When soaking at 520 °C, it takes less than 2 h for dispersoids to precipitate in the matrix [Fig. 7(a)], which is much faster than at 500 °C [Figs. 6(a) and 6(b)]. After 12 h, fine dispersoids with high number density are present [Fig. 7(b)]. With increasing holding time to 24 h [Fig. 7(c)], the size of dispersoid and number density keep increasing, indicating a full precipitation of dispersoids at this temperature. The two-step solution treatment is often preferably used in industrial production because of (i) avoiding possible incipient melting of Cu-containing phases and (ii) a short and effective solution treatment. As shown in Fig. 7(d) after 500 °C/4 h + 540 °C/2 h, the dispersoids are already precipitated with high number density but still with fine size. However, with increasing holding time of the second step, the size of α-dispersoids increases, as shown in Figs. 7(e) and 7(f), leading to a decrease in ΔHV after the peak value at 2 h (Fig. 5).

Tensile properties

For the role of α-dispersoids in mechanical properties, both experimental alloys were subjected to the optimum two-step solution treatment (500 °C/4 h + 540 °C/2 h), followed by an artificial aging at 200 °C for 5 h to fulfill the T7 temper. Typical stress–strain curves obtained for 356NM and 356M alloys at room temperature and at 300 °C are shown in Fig. 8. At room temperature [Fig. 8(a)], the values of yield strength (YS) and Ultimate tensile strength (UTS) obtained in both experimental alloys are comparable to those of commercial Al–Si 356 + Cu

https://doi.org/10.1557/jmr.2019.217 Published online by Cambridge University Press

© Materials Research Society 2019

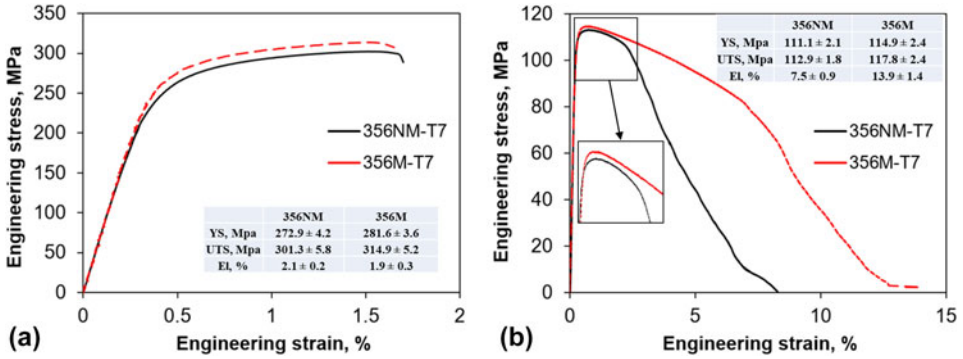


Figure 8: Typical stress–strain curves of experimental alloys at (a) room temperature and (b) 300 °C.

alloys (YS of 270–280 MPa and UTS of 300–320 MPa), which are mainly strengthened by the precipitation of nanoscale β′-Mg_2Si and θ′-Al_2Cu precipitates. On the other hand, compared with the base alloy (356NM), YS and UTS of 356M are found to be 8.7 MPa and 13.6 MPa higher, respectively, without sacrificing ductility. Since the addition of Mo has little influence on the formation of precipitates (β′ and θ′) during the aging treatment, it is reasonable to assume that the contribution of precipitates to the mechanical properties in both alloys is similar. Therefore, the improvement in the mechanical properties at room temperature of 356M alloy is principally from the formation of dispersoids, indicating a complementary strengthening contribution of α-dispersoids to alloy mechanical properties at room temperature. In 356M alloy, the presence of α-dispersoids can act as non-shearable obstacles to impede dislocation movement in the aluminum matrix, which are effective in Orowan bypass mechanism [26, 30], providing a small but extra strengthening. Meanwhile, the difference in microhardness between 356M and 356NM in T7 temper is measured to be 13 HV (112 HV versus 99 HV), which is similar to the difference in solution-treated condition (15 HV), indicating the stable contribution of dispersoids in both conditions.

At elevated temperature (300 °C), the YS and UTS of 356M alloy are 4 and 5 MPa higher than those 356NM alloy, mainly attributed to the formation of dispersoids in 356M alloy since the contribution to the elevated-temperature mechanical properties from precipitates (β′ and θ′) should be similar in both alloys. Though the improvement is not so remarkable (~5%) at this condition, it is expected to be more obvious during the long time service at 300 °C because the contribution of dispersoids is constant (4–5 MPa) due to their excellent thermal stability at 300–350 °C [13]. It is reported the YS of 356-T7 at 315 °C after 1000 h sharply decreases and remains only 24 MPa [34]. At long time service condition, the contribution of thermally stable dispersoids to YS will become remarkable, which would reach as high as 20% improvement on strength (4–5 MPa compared with 24 MPa) with 0.3% Mo addition in 356M alloy.

On the other hand, the elongation at 300 °C increases significantly from 7.5% (356NM) to 13.9% (356M) in Fig. 8(b). This can be also resulted from the dislocation–dispersoid interaction during the deformation. In the early stage of the tensile deformation, the dislocation density is low due to the elevated temperature [35], leading to the similar tensile behavior during elastic deformation at the beginning of test, as shown in Fig. 8(b). As the plastic deformation proceeds, dislocation density increases [36] and the effect of dislocation–dispersoid/precipitation interactions becomes more remarkable. Sitdikov et al. [37] noted a strong dislocation–dispersoid interaction during high temperature deformation and suggested that the dispersoids could trap the dislocations significantly. Furthermore, it is reported that the presence of dispersoids will change the slip system by means of cross-slip once the dislocation is blocked by dispersoids, making the homogenization of slip and then increasing the ductility [22, 23, 24]. On the other hand, it is also found that the homogeneous deformation is greatly promoted by converting the dislocation movement from the planar slip to a wavy slip mode through cross slip [24, 25], which also contributes to the improvement in the ductility. Therefore, it is reasonable to believe that the higher elongation in 356M than in 356NM in the present work can be likely also attributed to the formation of α-dispersoids.

The fracture surfaces after tensile tests at both room and elevated temperatures are shown in Fig. 9. As shown in Figs. 9(a) and 9(b) at room temperature, the fractures in both 356NM and 356M alloys exhibit typical mixed cellular fracture, reflecting the similar tensile behavior of both alloys at room temperature. Figures 9(c) and 9(d) show the fracture surfaces of the tested samples at 300 °C. High volume of dimples can be observed in both experimental alloys [Figs. 9(c) and 9(d)], exhibiting the ductile tensile behavior. The formation of dimples is the result of the void nucleation and subsequent coalescence during tensile deformation [38, 39]. Comparing Fig. 9(d) with Fig. 9(c), a finer and more uniform dimple size distribution is observed in the 356M alloy than in 356NM alloy,

https://doi.org/10.1557/jmr.2019.217 Published online by Cambridge University Press

© Materials Research Society 2019

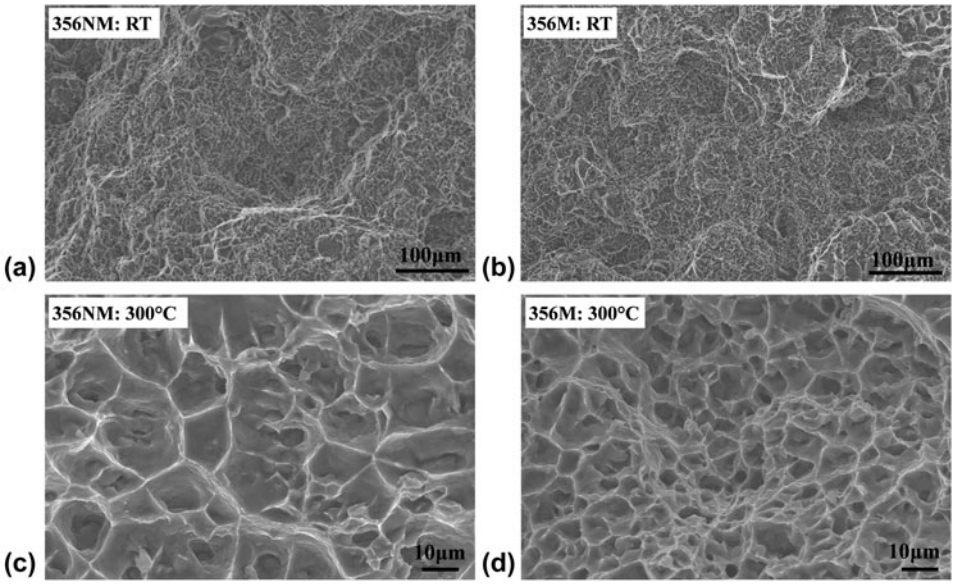


Figure 9: Tensile fracture surfaces of experimental alloys: (a, b) room temperature (RT) and (c, d) 300 °C; (a) and (c) is from 356NM alloy while (b) and (d) is from 356M alloy.

which can be attributed to a homogenous deformation due to the presence of dispersoids, leading to the higher elongation in 356M alloy. Furthermore, more energy needs to be consumed during the final fracture due to the high density of particle–matrix interfaces, thus resulting in better tensile toughness of 356M alloy [40].

As one of the most important properties at elevated temperature, the creep property of experimental alloys at T7 condition was also measured in the present work. The typical creep curves are shown in Fig. 10 obtained from compressive creep tests after 100 h. One thing to be mentioned is that the strain of 0.25 is the limit of the creep machine. As shown in Fig. 10, it takes 80 h to reach the strain of 0.25 in 356NM alloy, which is the maximum strain of the creep machine at compression mode, while strain reaches only 0.19 even after 100 h in 356M alloy. Besides, the minimum creep rates are calculated to be $1.3 \times 10^{-6}\ s^{-1}$ for 356NM alloy and $7.7 \times 10^{-7}\ s^{-1}$ for 356M alloy, representing 40% reduction of the minimum creep rate in the Mo-containing 356M alloy. In addition, the quasi-steady stage is indicated in Fig. 10, which is the most important stage during the creep test, especially the compression creep test [41]. It can be found that the time during the quasi-steady stage is only 30 h for 356NM but it is 58 h for 356 M, which is almost doubled in the alloy containing Mo. Therefore, it is also confirmed that the 356M alloy has much higher creep resistance than 356NM.

According to the creep condition applied in the present work (43.5 MPa at 300 °C), the creep mechanism is primarily controlled by the climb and glide of dislocations during creep deformation [41, 42]. Therefore, the creep resistance can be

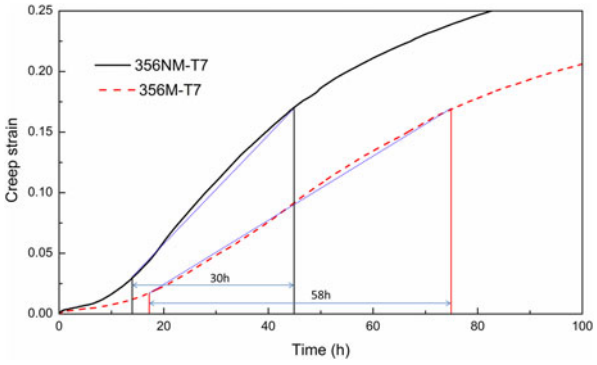


Figure 10: Typical compressive creep curves of experimental alloys at 300 °C with a constant load of 43.5 MPa with indicated quasi-steady stage.

affected by the factors that can interact with the movement of dislocations, including precipitates formed during aging treatment and dispersoids formed during the solution treatment. As mentioned above, both alloys in T7 condition are mainly strengthened by similar distribution of nanoscale β′-Mg_2Si and θ′-Al_2Cu precipitates. However, those precipitates show rapid coarsening at elevated temperature (300 °C), causing the decrease in strength of alloys with time. The difference between 356NM and 356M is the presence of a high number density of thermally stable dispersoids in 356M alloy, which can effectively hinder the movement of dislocations, resulting in a remarkable improvement in the creep resistance in 356M alloy.

As shown in Figs. 8 and 10, the formation of α-dispersoids due to the Mo addition provides an additional contribution to mechanical properties at both room and elevated temperatures.

https://doi.org/10.1557/jmr.2019.217 Published online by Cambridge University Press

© Materials Research Society 2019

It is well proven that the α-dispersoids are thermally stable at 300–350 °C [31], and therefore, the mechanical and creep properties of components made with Mo-containing 356 alloys can be less deteriorated during long time service at elevated temperature compared to conventional 356 alloys, providing a longer service life. On the other hand, it should be mentioned that the improvement of mechanical properties by the formation of α-dispersoids in the present experimental condition is marginal, although a reasonably high number of α-dispersoids were promoted by the addition of Mo and suitable heat treatment. In terms of strengthening mechanisms, the size of α-dispersoids precipitated (in the range of 100–150 nm) is still large and the number density is not high enough. To take the full advantage of thermally stable dispersoids in further increasing the mechanical properties particularly at elevated temperature, it remains a great challenge to refine dispersoids and to increase the volume fraction of dispersoids in the future work.

Conclusions

(1) With the addition of Mo in Al–Si–Mg 356-type alloy, the formation of α-dispersoids in the aluminum matrix during solution treatment was greatly promoted. A reasonably high number density of α-dispersoids were formed and distributed in the intradendritic region.

(2) The solution temperature had a strong effect on the precipitation kinetics of dispersoids in the Mo-containing 356 alloy. The formation of dispersoids started after 8 h at 500 °C and a full precipitation with increasing time occurred at 520 °C. At high temperature (540 °C), the coarsening of dispersoids with increasing time became predominant. The optimum conditions of dispersoids can be reached by 520 °C/12 h or 500 °C/4 h + 540 °C/2 h, leading to the highest differences in the microhardness.

(3) Due to a complementary strengthening contribution of α-dispersoids, the tensile strengths were improved at both room temperature and elevated temperature. The elongation was keeping similar at room temperature, while it was greatly improved at elevated temperature.

(4) The formation of thermally stable dispersoids due to the Mo addition also resulted in a remarkable improvement in the creep resistance with 40% reduction in the minimum creep rate.

Experimental procedures

In the present work, two experimental Al–Si–Mg 356-type alloys, defined as 356NM (the base alloy without Mo) and 356M with Mo addition, are prepared with commercially pure Al (99.7%), pure Mg (99.9%), Al–50% Si, Al–25% Mn, Al–50% Cu, Al–10% Sr, and Al–5% Ti–1% B master alloys. The chemical composition of 356NM is Al–7.27% Si–0.60% Cu–0.34% Mg–0.206Mn%–0.109% Fe–0.21% Ti–0.0113% Sr, while it is Al–6.99% Si–0.61% Cu–0.38% Mg–0.219Mn%–0.11% Fe–0.21% Ti–0.0113% Sr–0.30% Mo for 356M (all the composition is in wt% unless indicated otherwise).

For the casting process, pure Al and master alloys were melted and stirred to homogenize in clay-graphite crucible at 780 °C in an electric resistance furnace with protective atmosphere. The temperature of the melt was maintained at 780 °C for 30 min and then was degassed for 15 min. Finally, the liquid alloys were cast into a standard ASTM B-108 permanent mold preheated at 400 °C.

To evaluate the precipitation behavior of dispersoids, isothermal solution treatment was first applied in the temperature range of 500–540 °C, with a heating rate of 5 °C/min and with various soaking times up to 24 h. In addition, the two-step solution treatment (soaking 4 h at 500 °C, followed by 2, 4, 8, and 12 h at 540 °C) was also performed in the present work. The heating rate was 5 °C/min, and all the samples after solution treatments were quenched in water at room temperature for the metallographic observation and microhardness test. On the other hand, the samples for tensile and creep tests were further aged at 200 °C for 5 h to fulfill the industrial T7 temper. The tensile samples were machined following the ASTM E8 standard. The samples had a gauge length of 60 mm and a diameter of 13 mm. Tensile tests were performed by an Instron 8801 (Instron, Norwood, Massachusetts) servo-hydraulic testing system at a strain rate of 5×10^{-2} s^{-1}. Both 356NM and 356M alloys were tested at room temperature and elevated temperature (300 °C), and the tensile properties were obtained from the average value of three test samples. For the tensile temperature at 300 °C, the heating process is controlled by three-zone furnace equipped on the tensile-test machine and time to reach 300 °C is 20 min and then the sample was held at 300 °C for 5 min to stabilize. In addition, creep samples with cylindrical gauge length of 15 mm and diameter of 10 mm were machined. Compression creep tests were conducted at 300 °C for 100 h under a constant load of 43.5 MPa.

After casting and solution treatments, the specimens were polished for metallographic examination. 0.5% Hydrofluoric acid (HF) etching solution was used to reveal the distribution of dispersoids. An optical microscopy (Nikon Eclipse ME600, Tokyo, Japan) and an SEM (JEOL JSM-6480LV, Tokyo, Japan) equipped with EDS were used to investigate intermetallic phases and dispersoids. Vickers microhardness tests were performed on polished samples before etching (at least 15 tests for each sample) using a hardness tester (NG1000-CCD, Vancouver, Canada) with dwell time of 15 s and 25 g force at room temperature. During the hardness tests, the

https://doi.org/10.1557/jmr.2019.217 Published online by Cambridge University Press

© Materials Research Society 2019

indentations are guaranteed inside the dendrites without touching the intermetallics formed during the solidification to show the evolution of hardness from the aluminum matrix. The characters of dispersoids, including the average size and number density, were measured from SEM images at 1000×. At least five views were characterized, which contained more than few hundreds of dispersoids, ensuring that the statistical calculation is reliable and repeatable. A TEM (JEOL JEM-2100, Tokyo, Japan) equipped with an EDS was operated at 200 kV to confirm the morphology and chemical composition of dispersoids.

Acknowledgments

The authors acknowledge the financial support of the Natural Sciences and Engineering Research Council of Canada (NSERC) and Rio Tinto Aluminum through the NSERC Industry Research Chair in the Metallurgy of Aluminum Transformation at the University of Quebec at Chicoutimi.

References

1. **G. Liu and D.B. Müller**: Addressing sustainability in the aluminum industry: A critical review of life cycle assessments. *J. Cleaner Prod.* **35**, 108–117 (2012).
2. **T. Norgate, S. Jahanshahi, and W. Rankin**: Assessing the environmental impact of metal production processes. *J. Cleaner Prod.* **15**, 838–848 (2007).
3. **T. Team**: *Trends in Steel Usage in the Automotive Industry* (Forbes, 2015). Available at: https://www.forbes.com/sites/greatspeculations/2015/05/20/trends-in-steel-usage-in-the-automotive-industry/#4cd522114762.
4. **G. Cole and A. Sherman**: Light weight materials for automotive applications. *Mater. Charact.* **35**, 3–9 (1995).
5. **H. Ye**: An overview of the development of Al–Si-alloy based material for engine applications. *J. Mater. Eng. Perform.* **12**, 288–297 (2003).
6. **M. Garat and G. Laslaz**: Improved aluminum alloys for common rail diesel cylinder heads. *AFS Trans.* **115**, 89–96 (2007).
7. **F. Feikus**: Optimization of Al–Si cast alloys for cylinder head applications. *AFS Trans.* **106**, 225–231 (1998).
8. **M. Murayama and K. Hono**: Pre-precipitate clusters and precipitation processes in Al–Mg–Si alloys. *Acta Mater.* **47**, 1537–1548 (1999).
9. **Y. Li, S. Brusethaug, and A. Olsen**: Influence of Cu on the mechanical properties and precipitation behavior of AlSi7Mg0. 5 alloy during aging treatment. *Scr. Mater.* **54**, 99–103 (2006).
10. **G. Sha, H. Möller, W.E. Stumpf, J. Xia, G. Govender, and S. Ringer**: Solute nanostructures and their strengthening effects in Al–7Si–0.6 Mg alloy F357. *Acta Mater.* **60**, 692–701 (2012).
11. **K. Matsuda, S. Taniguchi, K. Kido, Y. Uetani, and S. Ikeno**: Effects of Cu and transition metals on the precipitation behaviors of metastable phases at 523 K in Al–Mg–Si alloys. *Mater. Trans.* **43**, 2789–2795 (2002).
12. **S. Wang, K. Matsuda, T. Kawabata, T. Yamazaki, and S. Ikeno**: Variation of age-hardening behavior of TM-addition Al–Mg–Si alloys. *J. Alloys Compd.* **509**, 9876–9883 (2011).
13. **K. Liu and X-G. Chen**: Development of Al–Mn–Mg 3004 alloy for applications at elevated temperature via dispersoid strengthening. *Mater. Des.* **84**, 340–350 (2015).
14. **K. Liu and X-G. Chen**: Evolution of intermetallics, dispersoids, and elevated temperature properties at various Fe contents in Al–Mn–Mg 3004 alloys. *Metall. Mater. Trans. B* **47**, 3291–3300 (2016).
15. **A.M.F. Muggerud, E.A. Mørtsell, Y. Li, and R. Holmestad**: Dispersoid strengthening in AA3xxx alloys with varying Mn and Si content during annealing at low temperatures. *Mater. Sci. Eng., A* **567**, 21–28 (2013).
16. **L. Ratke and P.W. Voorhees**: *Growth and Coarsening: Ostwald Ripening in Material Processing* (Springer, Berlin, London, 2013).
17. **R. Chen, Q. Xu, Z. Jia, and B. Liu**: Precipitation behavior and hardening effects of Si-containing dispersoids in Al–7Si–Mg alloy during solution treatment. *Mater. Des.* **90**, 1059–1068 (2016).
18. **Y. Li, A. Muggerud, A. Olsen, and T. Furu**: Precipitation of partially coherent α-Al (Mn, Fe) Si dispersoids and their strengthening effect in AA 3003 alloy. *Acta Mater.* **60**, 1004–1014 (2012).
19. **L. Lodgaard and N. Ryum**: Precipitation of dispersoids containing Mn and/or Cr in Al–Mg–Si alloys. *Mater. Sci. Eng., A* **283**, 144–152 (2000).
20. **H.Y. Kim, T.Y. Park, S.W. Han, and H.M. Lee**: Effects of Mn on the crystal structure of α-Al (Mn, Fe) Si particles in A356 alloys. *J. Cryst. Growth* **291**, 207–211 (2006).
21. **Y. Li and L. Arnberg**: Quantitative study on the precipitation behavior of dispersoids in DC-cast AA3003 alloy during heating and homogenization. *Acta Mater.* **51**, 3415–3428 (2003).
22. **S.W. Nam and D.H. Lee**: The effect of Mn on the mechanical behavior of Al alloys. *Met. Mater. Int.* **6**, 13 (2000).
23. **D.S. Park and S.W. Nam**: Effects of manganese dispersoid on the mechanical properties in Al–Zn–Mg alloys. *J. Mater. Sci.* **30**, 1313–1320 (1995).
24. **K. Kim and S.W. Nam**: Effects of Mn-dispersoids on the fatigue mechanism in an Al–Zn–Mg alloy. *Mater. Sci. Eng., A* **244**, 257–262 (1998).
25. **D. Lee, J. Park, and S.W. Nam**: Enhancement of mechanical properties of Al–Mg–Si alloys by means of manganese dispersoids. *Mater. Sci. Technol.* **15**, 450–455 (1999).
26. **A. Farkoosh, X.G. Chen, and M. Pekguleryuz**: Dispersoid strengthening of a high temperature Al–Si–Cu–Mg alloy via Mo addition. *Mater. Sci. Eng., A* **620**, 181–189 (2015).
27. **A. Farkoosh, X.G. Chen, and M. Pekguleryuz**: Interaction between molybdenum and manganese to form effective dispersoids

https://doi.org/10.1557/jmr.2019.217 Published online by Cambridge University Press

© Materials Research Society 2019

in an Al–Si–Cu–Mg alloy and their influence on creep resistance. *Mater. Sci. Eng., A* **627**, 127–138 (2015).

28. **C.M. Dinnis, J.A. Taylor, and A.K. Dahle**: As-cast morphology of iron-intermetallics in Al–Si foundry alloys. *Scr. Mater.* **53**, 955–958 (2005).
29. **S. Seifeddine, S. Johansson, and I.L. Svensson**: The influence of cooling rate and manganese content on the β-Al5FeSi phase formation and mechanical properties of Al–Si-based alloys. *Mater. Sci. Eng., A* **490**, 385–390 (2008).
30. **A. Farkoosh and M. Pekguleryuz**: Enhanced mechanical properties of an Al–Si–Cu–Mg alloy at 300 °C: Effects of Mg and the Q-precipitate phase. *Mater. Sci. Eng., A* **621**, 277–286 (2015).
31. **K. Liu, H. Ma, and X-G. Chen**: Enhanced elevated-temperature properties via Mo addition in Al–Mn–Mg 3004 alloy. *J. Alloys Compd.* **694**, 354–365 (2017).
32. **Y. Li and L. Arnberg**: Evolution of eutectic intermetallic particles in DC-cast AA3003 alloy during heating and homogenization. *Mater. Sci. Eng., A* **347**, 130–135 (2003).
33. **K.E. Knipling, D.C. Dunand, and D.N. Seidman**: Criteria for developing castable, creep-resistant aluminum-based alloys—A review. *Z. Metallkd.* **97**, 246–265 (2006).
34. **J.G. Kaufman**: *Properties of Aluminum Alloys: Tensile, Creep, and Fatigue Data at High and Low Temperatures* (ASM international, Materials Park, Ohio, 1999).
35. **W-S. Lee and Y-C. Huang**: Mechanical properties and dislocation substructure of 6061-T6 aluminum alloy impacted at cryogenic temperatures. *Mater. Trans.* **57**, 344–350 (2016).
36. **H. Adachi, Y. Miyajima, M. Sato, and N. Tsuji**: Evaluation of dislocation density for 1100 aluminum with different grain size during tensile deformation by using in situ X-ray diffraction technique. *Mater. Trans.* **56**, 671–678 (2015).
37. **O. Sitdikov, E. Avtokratova, T. Sakai, and K. Tsuzaki**: Ultrafine-grain structure formation in an Al–Mg–Sc alloy during warm ECAP. *Metall. Mater. Trans. A* **44**, 1087–1100 (2013).
38. **W. Wang, Y. Ma, M. Yang, P. Jiang, F. Yuan, and X. Wu**: Strain rate effect on tensile behavior for a high specific strength steel: From quasi-static to intermediate strain rates. *Metals* **8**, 11 (2017).
39. **D. Fang, Q. Duan, N. Zhao, J. Li, S. Wu, and Z. Zhang**: Tensile properties and fracture mechanism of Al–Mg alloy subjected to equal channel angular pressing. *Mater. Sci. Eng., A* **459**, 137–144 (2007).
40. **M. Warmuzek**: *Aluminum–Silicon Casting Alloys: An Atlas of Microfractographs* (ASM international, Materials Park, Ohio, 2004).
41. **L. Pan, K. Liu, F. Breton, and X.G. Chen**: Effect of Fe on microstructure and properties of 8xxx aluminum conductor alloys. *J. Mater. Eng. Perform.* **25**, 5201–5208 (2016).
42. **G.E. Dieter and D.J. Bacon**: *Mechanical Metallurgy* (McGraw-Hill, New York, 1986).

https://doi.org/10.1557/jmr.2019.217 Published online by Cambridge University Press

© Materials Research Society 2019